

Structural, dielectric and ferroelectric studies of thermally stable and efficient energy storage ceramic material: $(\text{Na}_{0.5-x}\text{K}_x\text{Bi}_{0.5-x}\text{La}_x)\text{TiO}_3$

Anita Verma¹, Arun Kumar Yadav¹, Nasima Khatun², Sunil Kumar¹, Ravindra Jangir³, Velaga Srihari⁴, V. Raghavendra Reddy⁵, Shun Wei Liu⁶, Sajal Biring^{6*}, Somaditya Sen^{1,2,6*}

¹Discipline of Metallurgy Engineering and Materials Science, Indian Institute of Technology Indore, Simrol, Indore 453552, India

²Department of Physics, Indian Institute of Technology Indore, Simrol, Indore 453552, India

³Synchrotrons utilization section, Raja Ramanna centre for advanced technology, Indore-452013

⁴High Pressure & Synchrotron Radiation Physics Division, Bhabha Atomic Research Centre, 400085, Mumbai, India

⁵UGC-DAE Consortium for Scientific Research, University Campus, Khandwa Road, Indore-452001, India

⁶Electronic Engg., Ming Chi University of Technology, New Taipei City, Taiwan

Abstract

The structural, dielectric and ferroelectric properties of lead-free $(\text{Na}_{0.5-x}\text{K}_x\text{Bi}_{0.5-x}\text{La}_x)\text{TiO}_3$ ($0 \leq x \leq 0.12$) powders synthesized by sol-gel self-combustion method were investigated. Rietveld refinement of Synchrotron x-ray diffraction (SXRD) data confirms pure single phase rhombohedral crystal structure with $R\bar{3}c$ space group for all the compositions and anti-phase ($a\bar{a}a\bar{a}$) octahedral tilting angle decreased with increase in composition x . Homogeneity and elemental proportions were confirmed by Energy dispersive x-ray spectrometry (EDS). The temperature-dependent dielectric study has shown two diffuse type of dielectric anomaly for all the samples, due to A-site disorder in the lattice, which has been assigned to two-phase transitions: ferroelectric to anti-ferroelectric and anti-ferroelectric to the paraelectric phase transition. The transition temperature of these phase transitions is found to decrease as a function of composition (x). Thermal stability range (ΔT) of dielectric constant increases from ~ 100 °C to 220 °C as a function of composition (x). Stable dielectric constant first increases, from 1557 ± 10 % for parent compound, with the composition, highest for $x = 0.06$ composition with $\epsilon_{\text{mid}} \sim 2508 \pm 10$ % for the temperature range ~ 180 °C to 340 °C, and after that decreases to 1608 ± 10 % for $x = 0.12$, but remain higher than the parent compound $\text{Na}_{0.5}\text{Bi}_{0.5}\text{TiO}_3$ (NBT). Ferroelectric measurements have shown monotonously decreasing coercive field (E_c) as a function of the composition due to decrease in grain size, confirmed by microstructural studies using Field Emission Scanning Electron Microscope (FESEM). Exponential increases in the energy storage efficiency (η) from ~ 17 % to 87 % as a function of composition (x) have also observed. These types of materials, with stable high dielectric constant (ϵ_r) and low loss ($\tan\delta$), have a vast scope in the field of the thermally stable dielectric constant materials and energy storage applications.

Keywords: - Lead-free dielectric, stable dielectric constant, Phase transition, Energy storage material, A-Site disorder, octahedral tilt

Introduction

In recent times, lead-free dielectric materials are gained much attention, due to the toxicity of lead-based materials, with thermally stable dielectric constant ($>200\text{ }^{\circ}\text{C}$) and low dielectric loss. These materials are extensively used as a capacitor where heat dissipation is a major issue mainly in electronic devices used in a harsh environment. Ceramic capacitors with fast charging and discharging rate, better mechanical and thermal properties, which are competitive to battery and other power storage devices [1], though, energy storage density of the ceramic capacitor is less in comparison to the battery. This new type of capacitor materials is used in sensing and controlling system of aerospace, aviation and automotive sectors in where controlling and sensing systems are placed closed to the engine at elevated temperature ($\sim 200\text{--}300\text{ }^{\circ}\text{C}$) [2]. These types of capacitor are also useful in down drilling in oil and gas industry in controlling and monitoring, where high-temperature stable electronics are required. Commercially available glass, polymer, and BaTiO_3 based materials are useful only below $200\text{ }^{\circ}\text{C}$ [3, 4], whereas, lead-based dielectric materials are used in $200\text{--}250\text{ }^{\circ}\text{C}$ temperature range. However, their toxicity and harmfulness to the environment necessitated to look for alternatives.

Sodium bismuth titanate, $\text{Na}_{0.5}\text{Bi}_{0.5}\text{TiO}_3$ (NBT), ceramics are one of the most promising lead-free alternatives, with ABO_3 type structure, dielectric and ferroelectric materials, discovered in 1960 [5, 6]. It has been used in many devices like sensor, actuators, pyroelectric infrared sensors, etc. [7-11]. NBT crystallizes with a perovskite-like structure with a sequence of phase transitions, a high-temperature NBT is in cubic (space group $Pm\bar{3}m$) structure which transforms to tetragonal (space group $P4bm$) (at $540\text{ }^{\circ}\text{C}$) and to room-temperature ferroelectric rhombohedral (space group $R3c$) structures (at $320\text{ }^{\circ}\text{C}$). NBT has A-site disordered structure due to heterovalent atoms at A-site $\text{Na}^+/\text{Bi}^{3+}$, where A-site equally shares by ferroelectric Bi^{3+} (50%) and inactive Na^+ (50%) [12, 13]. Bi^{3+} ions have “stereochemically active lone pair electrons”, a similar electronic configuration like Pb^{2+} [14], due to which Bi^{3+} has second-highest polarizability after Pb^{2+} [15]. At room temperature NBT has structural distortions due to hybridization between $\text{Bi}(6s^2)$ lone pairs and $\text{O}(2p)$ electrons, this distortion promotes large ferroelectricity and piezoelectricity in NBT [16-20]. This material has been explored during the past four decades due to its excellent dielectric and ferroelectric properties. It has relatively large remnant polarization, high Curie temperature $320\text{ }^{\circ}\text{C}$ and it also shows two diffuse type of dielectric anomaly with temperature, which is related to two-phase transition ferroelectric (FE) to anti-ferroelectric (AFE), and anti-ferroelectric (AFE) to paraelectric (PE). These phase transition temperatures become more diffuse by hetero-valent substitution at A or B-site in ABO_3 lattice system; this is claimed to be a possible reason behind stable dielectric constant in NBT [21, 22]. In this type of dielectric materials, temperature-dependent phase transitions (FE - AFE and AFE - PE) takes place in different micro-regions at different temperatures leads to diffusion of the dielectric peak [23]. These materials are used in the fields where thermally stable dielectric materials required. However, NBT has some drawbacks like high coercive field and leakage current, because of which poling is difficult. Many researchers tried A or B- site substitutions in NBT ceramic to improve its functionality [24]. Several reports are available in literature for

modified NBT material with thermally stable dielectric constant, $0.9(\text{Na}_{0.5}\text{Bi}_{0.5})\text{TiO}_3\text{-}0.1\text{KTaO}_3$ shows a stable dielectric constant ~ 1250 in wide temperature range -55 °C to 300 °C [25], Zr modified $\text{Na}_{0.5}\text{Bi}_{0.5}\text{TiO}_3\text{-}\text{Ba}_{0.8}\text{Ca}_{0.2}\text{TiO}_3\text{-}\text{NaNbO}_3$ shows a stable dielectric constant ~ 1300 in wide temperature range 80 °C to 280 °C [26], Ca modified $\text{Na}_{0.5}\text{Bi}_{0.5}\text{TiO}_3\text{-}\text{BaTiO}_3$ shows a stable dielectric constant ~ 1300 in wide temperature range -50 °C to 200 °C [21].

From above discussion, it is evident to note that substitution at A or B-sites in NBT by different anions create disorder in the lattice, which leads to various interesting phenomena. Electronic polarizability (α_D) of *La* ($\alpha_D \sim 170 - 214$) and *K* ($\alpha_D \sim 289 - 294$) is larger than *Bi* ($\alpha_D \sim 50-60$) and *Na* ($\alpha_D \sim 161 - 163$) respectively [27], apart from this, average crystal radius of K^+ (1.78 Å) and La^{3+} (1.5 Å) is almost comparable to Na^+ (1.53 Å) and Bi^{3+} (1.52 Å), there is a probability of A-site substitution in parent compound NBT. This may lead to increase in the dielectric constant of the NBT compound. It is also reported that doping of rare-earth metal La^{3+} suppress the grain growth which reduces coercive field (E_c) [28]. Thus, the motivation of this work is to explore the effect of substitution of $\text{K}^+/\text{La}^{3+}$ on A-site in place of *Na/Bi* on structural, morphology, dielectric and ferroelectric properties. For this, $(\text{Na}_{0.5-x}\text{K}_x\text{Bi}_{0.5-x}\text{La}_x)\text{TiO}_3$, ($0 \leq x \leq 0.12$) were synthesized by sol-gel method. Thermally stable dielectric constant and also high energy storage efficiency 87% was observed for $x = 0.12$ composition. This material system can be useful in high-temperature stable capacitors beyond operating temperature >200 °C and efficient energy storage applications.

Experimental

A series of polycrystalline $(\text{Na}_{0.5-x}\text{K}_x\text{Bi}_{0.5-x}\text{La}_x)\text{TiO}_3$, ($x = 0, 0.03, 0.06, 0.09$, and 0.12) [abbreviated as NKBLT- x] powders were prepared using sol-gel self-combustion method. All the precursors used in the synthesis are purchased from Alfa Aesar and used without further purification. Precursors selected to synthesize NKBLT- x were sodium nitrate (purity 99.9%), bismuth nitrate (purity 99.9%), dihydroxy-bis (ammonium lactate) titanium (IV) (50% w/w aqua solution (purity 99.9%)), potassium nitrate (purity 99.9%), and lanthanum nitrate (purity 99.9%). These precursors were selected due to their solubility in deionized (DI) water. Bismuth nitrate is not soluble in DI water but is soluble in dilute HNO_3 . Stoichiometric solutions of each precursor were prepared with DI water in separate beakers. Titanium solutions were mixed in lanthanum solutions, followed by bismuth, sodium, and potassium. These mixed solutions (precursors) were stirred for 2 h on a magnetic stirrer at room temperature. Solutions of ethylene glycol and citric acid of 1:1 molar ratio were prepared in separate beakers as fuel. The fuel solution was added to precursor solution and stirred vigorously, the ratio of oxidizer to the fuel was calculated using the standard procedure mentioned elsewhere [29]. The resultant solution was continuously stirred and heated to form the gel at ~ 85 °C. The gel was burnt in a fume hood on the hot plate to form dark brown powders. These powders were further heated at 450 °C for 12 h for denitrification and de-carbonization. The resultant powders were calcined at 700 °C for 10 h after grinding in mortar and pestle. These powders were mixed with 5 weight % polyvinyl alcohol solution (binder) and pelletized with a uni-axial press into discs of ~ 13 mm diameter and ~ 1.5 mm

thickness. The binder was burnt off at 600 °C for 6 h. Further sintering continued at 1150 °C for 3 h to form dense pellets.

Synchrotron powder x-ray diffraction (SRPXRD) measurements were carried out on the ensuing powders, at ambient conditions, at Extreme Conditions Angle Dispersive/Energy Dispersive X-Ray Diffraction (EC-AD/ED-XRD) Beam Line-11 (BL-11) at Indus-2 synchrotron source, RRCAT, Indore, India. Measurements were performed in rotating capillary mode at ~150 rpm to reduce orientation effects. Diameters of capillary tubes were selected taking into account the linear absorption coefficient of samples and 25% packing density of material in a capillary. The desired wavelength, $\lambda = 0.50346 \text{ \AA}$, for ADXRD diffraction experiments was selected from the white light of the bending magnet using a Si(111) channel-cut monochromator. The monochromatic beam is then focused on to the samples with a Kirkpatrick-Baez (K-B) mirror. A MAR345 image plate detector (which is an area detector) was used to collect two-dimensional diffraction data. The sample to detector distance and wavelength of the beam were calibrated using NIST standards CeO₂ and LaB₆. Calibration and conversion/integration of 2D diffraction data to 1D, intensity versus 2θ, was carried out using FIT2D software [30]. Microstructure and elemental analysis of sintered pellets were investigated by Supra55 Zeiss field emission scanning electron microscope equipped with energy dispersive x-ray spectrometer (EDS). Experimental bulk densities, ρ_e , of NKBLT- x pellets were estimated by Archimedes' methods using Xylene (density=0.86 g/cm³) as the liquid media. Electrodes were prepared using high-temperature silver paste for electrical property measurements. Silver paste was painted on both sides of sintered pellets. These pellets were cured at 550 °C for 15 min. To avoid moisture content in the samples finally, the pellets were annealed at 200 °C for 15 min before electrical measurements. The dielectric response was measured using a Newtons 4th LTD phase sensitive multimeter with the signal strength of 1V_{rms}. A ferroelectric loop (P-E) tracer of M/s Radiant Instruments, USA was used to perform ferroelectric (P-E) loop measurements on sintered pellets immersed in silicone oil (to prevent electric arcing at high voltages).

Results and Discussion

Measured SRPXRD patterns of NKBLT- x powders are shown in Fig.1. Preliminary analysis of the SRPXRD patterns shows that all the samples are in rhombohedral structure with R3c space group as reported in the case of parent NBT. Insets in Fig. 1 shows enlarged the portion of the SRPXRD pattern for Bragg peaks (110) and (113), though similar changes are observed with other Bragg reflections as well, we showed these Bragg peaks as a representation. It is seen from the Bragg peak (110), that the diffraction peak shifts to lower 2theta as the value of x increases, which indicated lattice expansion in *ab*-plain. Observation of (113) Bragg peak (inset in Fig. 1) indicated that with the increase in substitution, the intensity of superlattice reflection (113) decreases, and for $x = 0.12$ composition this peak disappeared.

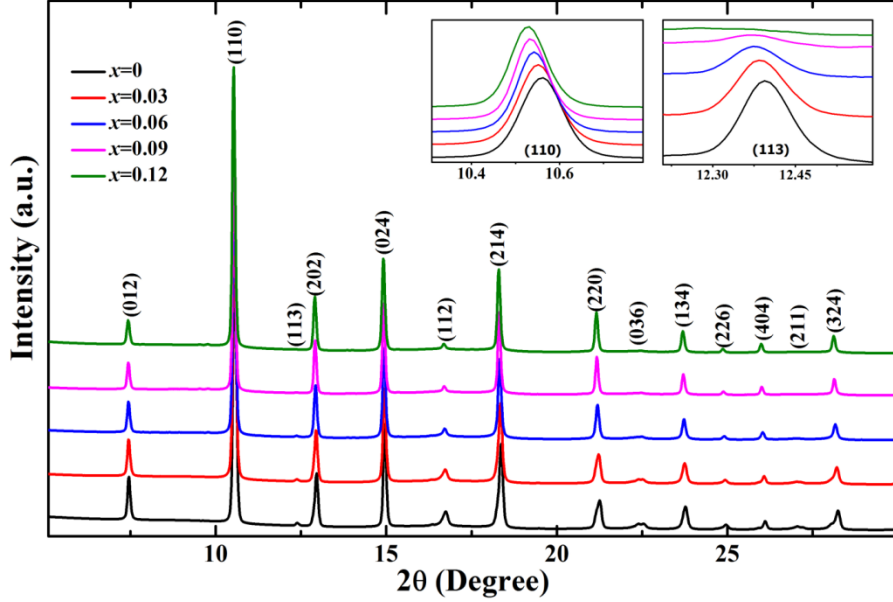


Figure 1. (a) Synchrotron powder XRD pattern of $(Na_{0.5-x}K_xBi_{0.5-x}La_x)TiO_3$, ($0 \leq x \leq 0.12$), samples showing dominant NBT structure for pure and substituted samples. (Inset) Peak shifting of (110) to lower 2θ with the increasing substitution implying lattice expansion, and (inset) Peak (113) is disappeared with increase in K/La substitution implying that increase in lattice disorder and suppression in octahedral tilting.

In General crystal structure of NBT is described by rhombohedral unit cell (with $R\bar{3}c$ space group) by cation displacement along [111] with anti-phase tilting of (TiO_6) octahedral, whereas, Megwan and Darlington chose hexagonal axis (a_H and c_H) for refinement of rhombohedral $R\bar{3}c$ unit cell with the lattice transformation as shown in table 1. Where, ‘t’ and ‘s’ are defined as the polar cationic displacement, ‘d’ as the octahedral distortion and ‘e’ as rotation of an octahedron face about the triad axis [31].

Table 1. Fractional coordinates for the hexagonal setting of rhombohedral ($R\bar{3}c$ space group) perovskite.

Atom	Wyckoff site	x	y	z
$Na/K/Bi/La$	6a	0	0	0.25+s
Ti	6a	0	0	t
O	18b	1/6-2e-2d	1/3-4d	1/12

In order to find out the structural variation with the substitution, we have carried out Rietveld refinement of SRPXRd data using Fullprof software for all the composition [32], and results are presented in Fig. 2. Voigt axial divergence asymmetry function was used to model the Bragg peaks. The background was estimated by linear interpolation between selected background points. Scale parameter, lattice parameters (a , b , c), half-width parameters (U , V , W),

position parameters of various lattice sites (x, y, z) (Table 1) (with z position of O taken fix at 1/12), and thermal parameter B_{iso} (isotropic Debye-Waller factor) were refined one by one. A goodness of refinement is obtained after refining preferred orientation and asymmetric parameters. Acceptable R-factor R_{wp} , and R_{exp} were obtained for all compositions. Rietveld refinement of samples with $x = 0, 0.06$ and 0.12 compositions along with R-factors of fit are shown in Fig. 2(a-c). From the Rietveld refinement, it is observed that the lattice parameters ‘ a ’ increases while ‘ c ’ decreases with increase in substitution (as shown in Fig. 2e). However, as shown in Fig. 2e the average unit cell volume increases with increase in substitution. The observed change in lattice parameters and overall volume may be due to the relative increase of effective ionic radii at A-site with increase in substitution, which is a clear indication of successful substitution at A-site of K^+/La^{3+} on the place of atoms Na^+/Bi^{3+} in NBT parent compound. Average crystal radii (r_A) of A-site cations in NBLT- x compositions were calculated using the following equations.

$$r_A = \frac{1}{2} * [(1 - x)(r_{Na^+} + r_{Bi^{3+}}) + x(r_{K^+} + r_{La^{3+}})] \quad (1)$$

Where, r_{Na^+} , r_{K^+} , $r_{Bi^{3+}}$, and, $r_{La^{3+}}$ crystal radii of Na^+ , K^+ , Bi^{3+} , and La^{3+} , respectively. To estimate the relative distortion in the unit cell with substitution, ‘ c/a ’ ratio was calculated. The ‘ c/a ’ ratio is found to decreases from 2.47 to 2.44 for $x = 0$ and 0.12 composition respectively; it implies that distortion is reduced in the unit cell with the increase in substitution. Distortion is related to the strength of chemical bonding between the constituent elements. Hybridization happens between $Ti(3d)$ and $O(2p)$ electrons. However, a stronger hybridization takes place between lone pair electrons of $Bi(6s^2)$ with $O(2p)$ electrons. This hybridization is responsible for ferroelectricity in NBT structure [16-20]. Both La and K do not have such lone pairs. As a result, the distortive factor is reduced. The estimated thermal parameter B_{iso} of A-site is found to increases from $2.18(3)$ \AA^2 to $3.55(5)$ \AA^2 for $x = 0$ and 0.12 composition respectively (as shown in Fig. 2f). Which imply that the configurational static disorder in A-site is increasing with the substitution of K^+/La^{3+} at the A-site [33].

While the tilt angle of octahedral ‘ ω ’ is given by $\tan\omega = 4*(3)^{1/2}e$ [34, 35]. Anti-phase ($a^-a^-a^-$) octahedral tilting angle ‘ ω ’ decreased from 8.47° to 5.89° for $x = 0$ and $x = 0.12$ composition respectively Fig. 2f (right). Moreover, the $Ti-O$ bond lengths are changes from 2.028 \AA and 1.877 \AA , to 1.971 \AA and 1.938 \AA for $x = 0$ and 0.12 composition respectively, it implies that distortion reduced with increase in substitution. In order to visualize changes in atomic positions and orientation of octahedral in a unit cell, the geometric structure is drawn using refined CIF file (Crystallographic Information File) for all composition by VESTA software [36]. As a representative for $x = 0$ and 0.12 structure has been seen from ($x y z$). In Fig 3a and b off-centering (distance between to cross dotted line center of A-site atom) of A-site atoms are shown, for $x = 0$ and 0.12 composition. It is observed that off-centering of A-site cation was more in parent composition comparatively to the $x = 0.12$ composition. Off-centering of A-site cation was played very important role in origin of ferroelectricity in perovskite materials[37]. In

fig. 3c and 3d have been shown octahedra rotation of $x = 0$ and 0.12 composition respectively, from these figures, it can be perceived that the octahedral tilt along the vertical direction in the figure reduced substantially. Figures 3c and 3d are drawn in the *ab*-plain seen from *c* axis [001], in this figure two octahedra's are seen one over the other, shows that the in-plain (*ab*-plain) rotation over the *c* axis reduced as the concentration of x increases (highlighted in the black circle).

As observed from SRPXRD, the intensity of Bragg reflection (113) decreases with increase in x , and for $x = 0.12$ composition, this peak disappeared. It has been reported that Bragg reflection (113) is related to octahedral tilting and long-range order [25, 34]. In our system, as reported earlier, the tilt angle ω changes from 8.47° to 5.89° for $x = 0$ to 0.12 composition respectively. All thought, there exist small tilt angle in $x = 0.12$ sample compared to the parent compound, the (113) reflection is disappeared; this may be due to the observed increased disorder at A-site in the system.

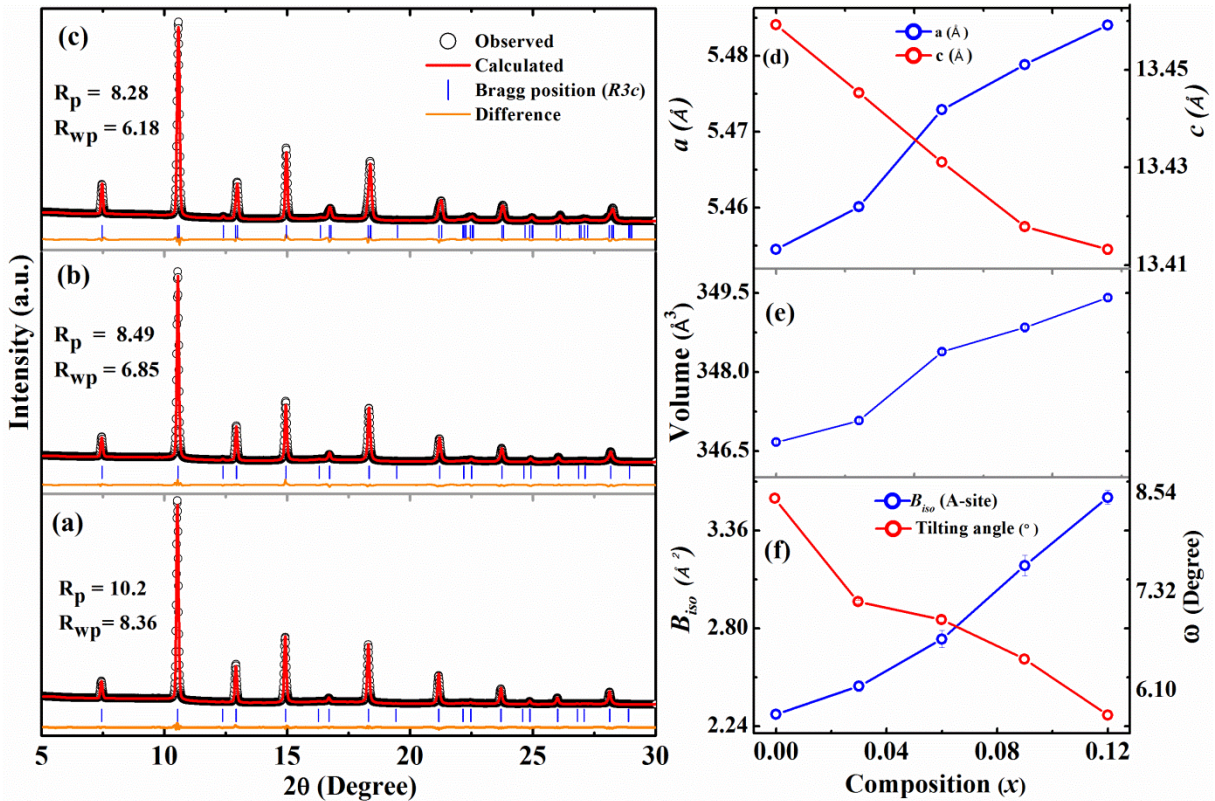


Figure 2. Rietveld refinement of SRPXRD data of $(\text{Na}_{0.5-x}\text{K}_x\text{Bi}_{0.5-x}\text{La}_x)\text{TiO}_3$, ($0 \leq x \leq 0.12$) with goodness of fitting after final cycle with parameters where, (a) $x = 0$, (b) $x = 0.06$ and (c) $x = 0.12$ compositions, (e) Lattice parameter of unit cell 'a' increases while 'c' decreases with substitution, (c) Increase in unit cell volume with substitution, and (d) B_{iso} (isotropic Debye-Waller factors) increases with composition may be lattice system more disordered (right), octahedral tilting angle decreases with composition (left),

Table 2. Atomic positions, and lattice parameters of $NKBLT-x$ with ($0 \leq x \leq 0.12$) ceramics refinement with $R3c$ space group, obtained after final cycle of refinement.

Atoms	Coordinates	0	0.03	0.06	0.09	0.12
$Na/Bi/K/La$	x	0	0	0	0	0
	y	0	0	0	0	0
	z	0.2730	0.2689	0.2570	0.2562	0.2514
Ti	x	0	0	0	0	0
	y	0	0	0	0	0
	z	0.009	0.0087	0.006	0.0034	0.0029
O	x	0.1265	0.1352	0.1387	0.1431	0.1480
	y	0.3392	0.3434	0.3481	0.3519	0.3546
	z	0.08333	0.08333	0.08333	0.08333	0.08333

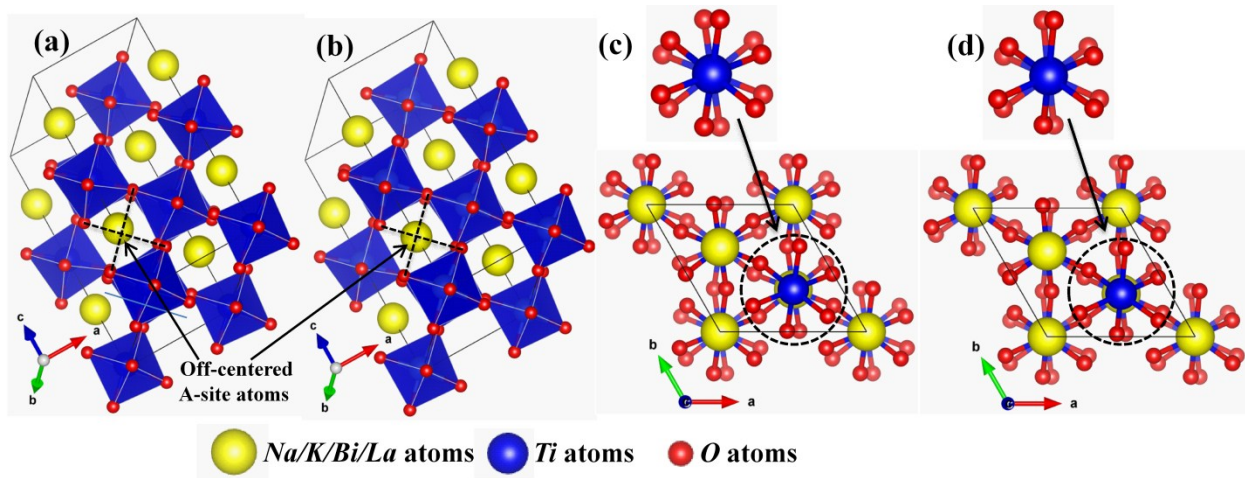


Figure 3. Unit cell structure with rhombohedral ($R3c$ space group) of perovskite ($Na_{0.5-x}K_xBi_{0.5-x}La_3$, ($0 \leq x \leq 0.12$) from different perspective , where (a,c) $x = 0$ composition (b,d) $x = 0.12$ composition octahedral tilting from projection from (xyz) and (00x) plain respectively, with composition octahedral tilting suppressed.

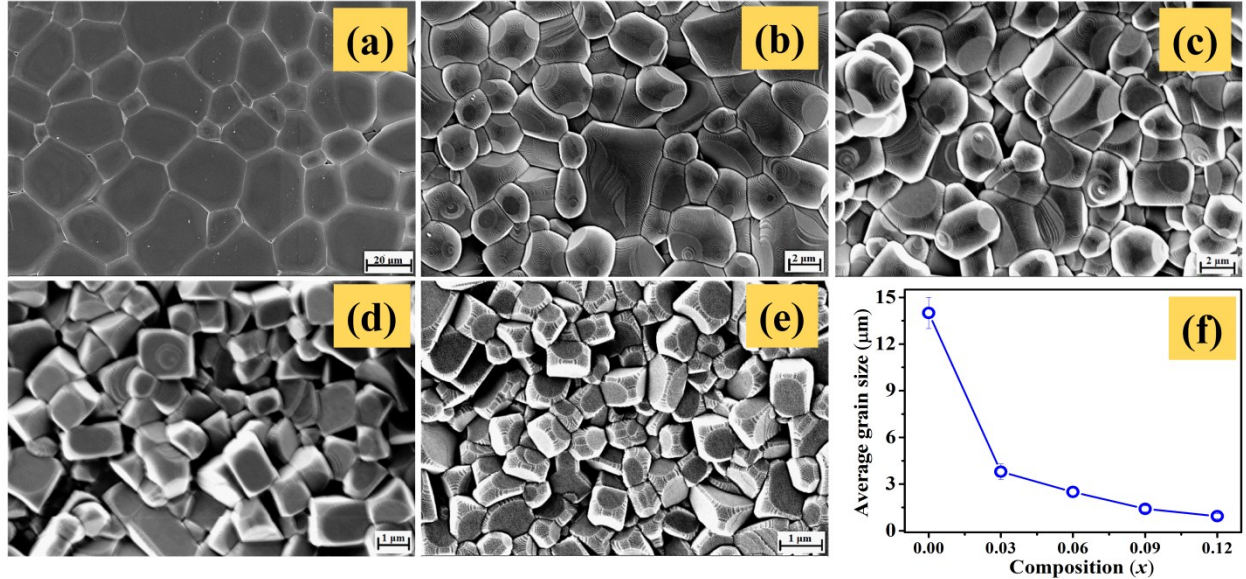


Figure 4: Surface morphology ($Na_{0.5-x}K_xBi_{0.5-x}La_xTiO_3$, $0 \leq x \leq 0.12$) compositions of sintered pellets showing reducing grain size of particles where (a) $x = 0$, (b) $x = 0.03$, and (c) $x = 0.06$, (d) $x = 0.09$, and (e) $x = 0.12$; (f) Average grain size variation with compositions.

Surface morphology of the $NKBLT-x$ sintered pellets, at 1150 $^{\circ}C$ for 3 h, was examined using FESEM [Fig. 4(a-e)]. It is clearly visible that, grains are close-packed for all composition. Average grain size was estimated using Image J software and was found to decrease from $14.01 \pm 0.99 \mu m$ to $0.94 \pm 0.15 \mu m$ for $x = 0$ to 0.12 respectively as shown in Fig.4f. It is well known that rare-earth elements, due to their low diffusivity, are inhibitors of grain growth. Substitution of K^+ in the place of Na^+ reduces the agglomeration resulted in substantial reduction in particle size. This indicates substituted ions of the large radius are more difficult to diffuse to facilitate grain growth and more efficient to suppress the grain growth than those of small radius [18, 28, 38]. Theoretical density (ρ_t) was calculated from the refinement of XRD data, and experimental density (ρ_e) was calculated from Archimedes' methods. Relative density ($\rho_R = \rho_e / \rho_t$), continually increasing ($x(0) \sim 91.5\%$, $x(0.03) \sim 92.4\%$, $x(0.06) \sim 93.7\%$, $x(0.09) \sim 94.9\%$, and $x(0.12) \sim 95.6\%$). Which shows that the suppressed grain growth helps in better densification [39].

EDS was performed on various regions of all the samples. A representative $NKBLT-0.12$ sample, as shown in Fig. 5(b-g), demonstrates the presence and homogenous distribution of Na , K , Bi , La , Ti and O without segregation over a selected area (shown in secondary electron micrograph). An integrated area spectrum and estimation of atomic and the weight percentage of constituent elements reveals a close match with stoichiometric composition taken for sample preparation [Fig. 5h].

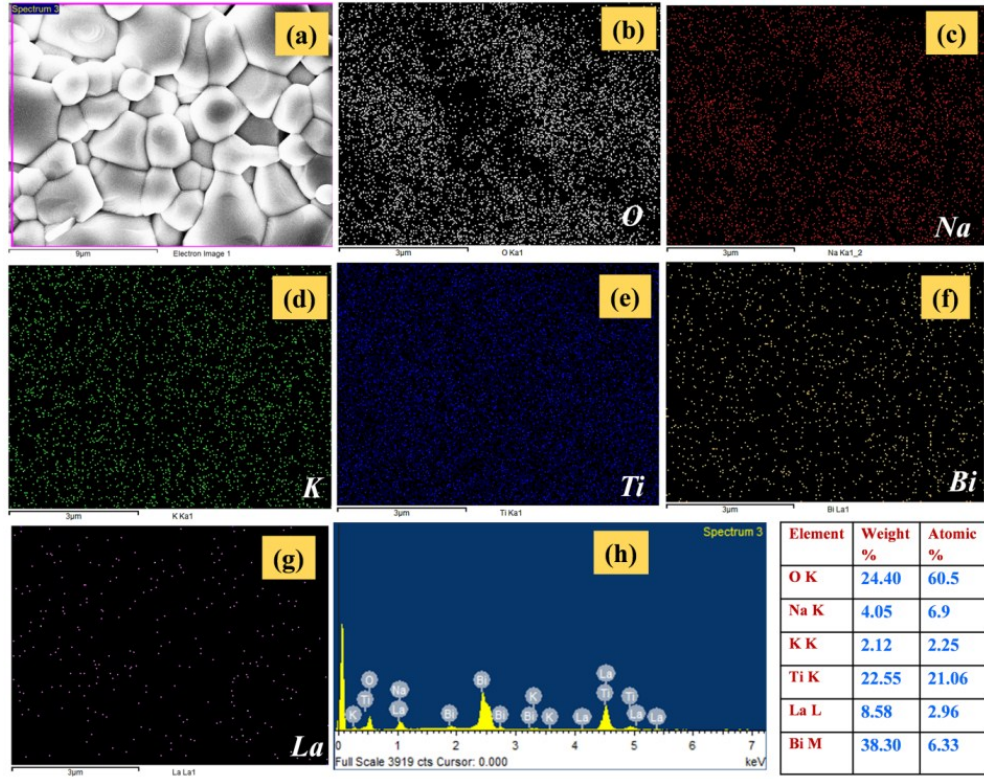


Figure 5. Elemental analysis of $(Na_{0.5-x}K_xBi_{0.5-x}La_x)TiO_3$ with $x = 0.12$ composition where (a) FESEM image, Elemental mapping of (b) O, (c) Na, (d) K, (e) Ti, (f) Bi, (g) La showing uniform compositional homogeneity. (h) Area EDS data showing all contributing ions also atomic and weight percentage of constituent elements (Table).

Room temperature frequency-dependent relative permittivity (ϵ_r) and dielectric loss ($\tan\delta$) of $NKBLT-x$ ($0 \leq x \leq 0.12$) samples were studied some fixed frequencies in 100Hz to 1MHz range. Both ϵ_r and $\tan\delta$ decreases with increase in frequency for all samples but increases with increasing substitution [Fig. 6(a-b)]. Polarization in the dielectric material is the sum of the contribution of electronic, ionic, orientation and space polarization, and it is strongly dependent on frequency. At lower frequency, all polarization contributes easily, but as the frequency is increased different polarization will filter out, this is the possible reason behind to decrease ϵ_r with frequency. With increase in composition the dielectric constant (ϵ_r) increases from ~ 250 to ~ 1095 , and dielectric loss ($\tan\delta$) slightly increases 0.024 to 0.065 for $x = 0$ and 0.12 composition respectively at 500 kHz frequency. Increasing ϵ_r with increasing substitution may be related to decreasing of the phase transition temperature with the increase in substitution (as shown in Fig. 7). Also, some contribution electronic polarizability (α_D) of La ($\alpha_D \sim 170 - 214$) and K ($\alpha_D \sim 289 - 294$) is higher than Bi ($\alpha_D \sim 50-60$) and Na ($\alpha_D \sim 161 - 163$) respectively.

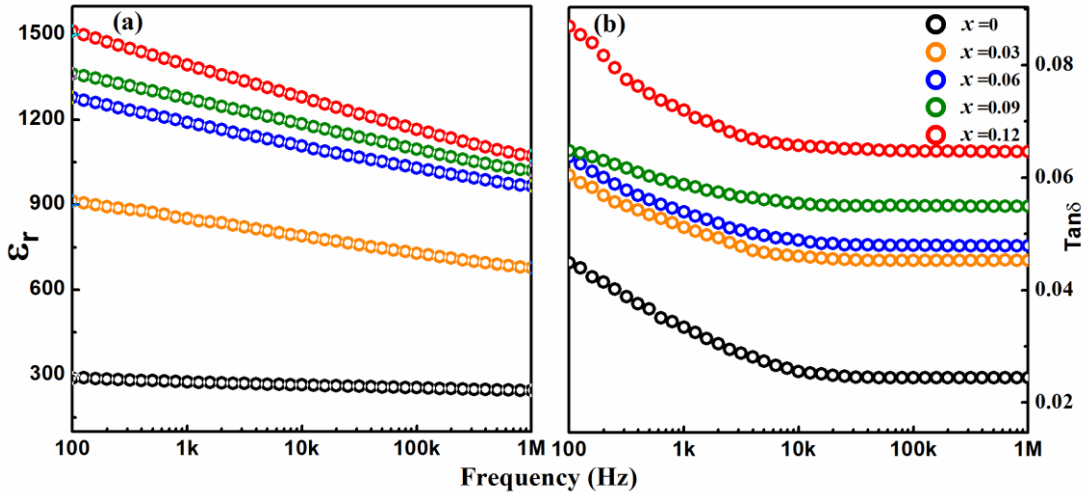


Figure 6.(a) Frequency-dependence of dielectric relative permittivity (ϵ_r) of $(Na_{0.5-x}K_xBi_{0.5-x}La_x)TiO_3$, ($0 \leq x \leq 0.12$) at room temperature showing increase of ϵ_r with substitution; (b) $\tan\delta$ of the samples increase with the substitution but reduces with frequency.

Phase transition temperature was investigated using dielectric properties as a probe. The temperature-dependent ϵ_r and $\tan\delta$ of $NKBLT-x$ samples were measured in the temperature range 50 °C to 450 °C for some fixed frequencies 100Hz to 1MHz, results of which are as shown in Fig. 7. Temperature-dependent ϵ_r shows that it increases up to a certain temperature and exhibits broad dielectric maxima around T_m . After that, ϵ_r reduces with increase in temperature above T_m . Generally, two broad anomalies observed in NBT, which are T_d and T_m . Temperature T_d referred to depolarization temperature and which is corresponding to FE to AFE phase transition temperature. Temperature T_m referred as the maximum dielectric constant temperature which corresponds to AFE to PE phase transition [Fig. 7(a-e)] [40, 41]. In K^+/La^{3+} substituted samples also two diffuse types of anomalies were observed in the temperature-dependent dielectric study, diffuseness of these anomalies increases with increase in substitution. These two phase transitions T_d , and T_m move towards lower temperatures with increasing substitution (as shown in Table. 3) from ~ 197 °C and 302 °C to 74 °C and 206 °C, for $x = 0$ and 0.12 composition respectively. Decreasing T_d and T_m with increasing substitution may be related to the reduction of distortion in lattice system. Distortion is related to the strength of chemical bonding between the constituent elements, the origin of distortion is the lone pair electrons of $Bi(6s^2)$, but La and K do not have such lone pairs. As a result, the distortive factor is reduced. From XRD data refinement, estimated ‘c/a’ ratio is also showing that distortion reduces with substitution. As a result, the distortive factor is reduced thereby reducing T_m . A comparison of phase transition temperature at 500 kHz for all the samples is shown in Fig.7g.

Diffuse phase transition exhibit a broad dielectric anomaly instead of a sharp dielectric anomaly at the Curie point, like normal ferroelectric materials $BaTiO_3$, $PbTiO_3$, etc. The phase transition characteristics of such materials are known to diverge from the characteristic Curie-

Weiss behavior and phase transition behavior explained by the modified Curie-Weiss law [42-44] given below:

$$\frac{1}{\epsilon'} - \frac{1}{\epsilon'_m} = C^{-1}(T - T_m)^\gamma \quad (2)$$

Where C is Curie-Weiss constant and γ gives the degree of diffuseness. For sharp phase transition behavior $\gamma = 1$ and for ideal diffuse phase transition $\gamma = 2$. The degree of diffuseness was calculated by the least square linear fitting of $\ln(\frac{1}{\epsilon'} - \frac{1}{\epsilon'_m})$ versus $\ln(T - T_m)$ curves at a frequency of 500 kHz for all the $(Na_{0.5-x}K_xBi_{0.5-x}La_x)TiO_3$ ceramic samples. Value of degree of diffuseness is increasing with substitution from 1.61 ± 0.02 to 1.97 ± 0.02 for $x=0$ and 0.12 composition (Table 3). Diffusions (γ) increased with composition x , possible reason behind this may be multiple relaxation processes arising from A-site lattice disorder, which have different transition temperatures. Thus, the enhanced A-site lattice disorder in the samples with K^+/La^{3+} substitution as observed in SRPXR (increase in thermal parameter B_{iso}) is the reason behind the diffused dielectric phenomenon in the samples [24]. However, as a result, these materials show a region of the steady dielectric constant with temperature. Region for stable dielectric constant, ΔT , is generally given by $\epsilon_{mid} \pm 15\%$ or better, where ϵ_{mid} is the value of stable dielectric constant. Temperature limits T_{Low} and T_{High} are defined as lower and higher temperatures as ($T_{Low} < T_m < T_{High}$), and T_m is the temperature corresponding to maximum dielectric constant ϵ_m [45]. A temperature region, ΔT , has been highlighted in yellow for $\epsilon_{mid} \pm 10\%$. ΔT increases with increasing substitution and thermal stability of ϵ_r for $x(0) \sim 280$ °C to 380 °C $x(0.12) \sim 80$ °C to 300 °C. This property makes these materials important to be utilized as high-temperature stable capacitor applications.

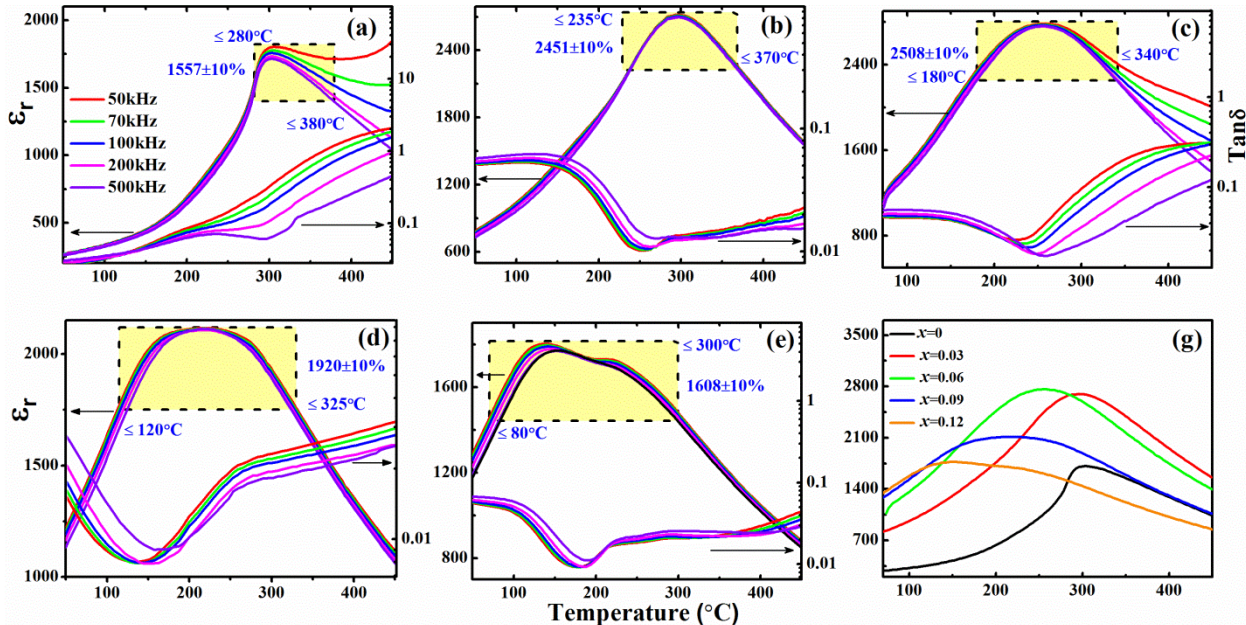


Figure 7. Temperature-dependent dielectric measurement of $(Na_{0.5-x}K_xBi_{0.5-x}La_x)TiO_3$, ($0 \leq x \leq 0.12$) samples for different frequencies; thermally stable region is highlighted (yellow): (a) $x = 0$, (b) $x = 0.03$, (c) $x = 0.06$, (d) $x = 0.09$, and (e) $x = 0.12$, (g) Variation in phase transitions for different substitution at 500kHz.

Table 3. Room temperature, high temperature dielectric and ferroelectric properties of $(Na_{0.5-x}K_xBi_{0.5-x}La_x)TiO_3$, ($0 \leq x \leq 0.12$)compositions

x	Room Temperature at 500kHz		T _d (°C)	T _m (°C)	High Temperature at 500kHz				
	ε _r	Tanδ			ε _m	Tanδ	γ	ε _{mid} ±10%	ΔT (°C)
0	250	0.024	197	302	1015	0.063	1.61±0.02	1557	280-380
0.03	690	0.045	173	296	2696	0.013	1.74±0.01	2451	235-370
0.06	980	0.047	151	253	2757	0.018	1.85±0.03	2508	180-340
0.09	1037	0.054	113	218	2112	0.011	1.94±0.03	1920	120-325
0.12	1095	0.065	74	206	1769	0.021	1.97±0.02	1608	80-300

* ΔT is temperature range for thermally stable dielectric constant ε_{mid}±10%

The dynamic hysteresis with the applied electric field in ferroelectric materials is intrinsically related to the dynamics of the polarization reversal under a cycle of a time-varying electric field, where the hysteretic polarization reversal behaviors are usually induced by domain wall motion and domain switching. Polarization, P , was measured as a function of applied *ac* electric field E (maximum electric field for all samples before breakdown), at a frequency of 1Hz at room temperature as shown in Fig. 8(a-e). It is observed from P-E loop measurement that increases in A-site substitution of K^+/La^{3+} , significantly effects the coercive field (E_c), remnant polarization (P_r) and maximum polarization (P_{Max}) given in Table 3. Coercive field (E_c) monotonously decreases with increasing substitution; it follows the same trend, the grain size with substitution. This reduction in E_c may be related to the reduction of grain size with substitution. Reduced coercive field with substitution may be due to decreased domain size and increased domain switching [46, 47]. In ferroelectric materials, softening of E_c is generally related to the variation in their domain size. Correlation between domain size (d) and grain size (t) is given by the following equation: [48, 49]

$$d = \left[\left(\frac{\sigma}{\epsilon^* P_0^2} \right) \cdot t \right] \quad (3)$$

Where, σ , ϵ^* and P_0 are the energy density of the domain wall, effective dielectric constant, and spontaneous polarization, respectively. It may be decrement in grain size is the possible reason

behind reduction in E_c . Pure NBT has high coercive field and leakage current. Therefore difficult to pole this sample, by K^+/La^{3+} substitution E_c was reduced. Thus easy to pole these samples, it is an advantage of these materials to use in electronics device. However, remnant polarization (P_r) first increases till $x = 0.06$ composition, after that it decreases.

P - E loops become slimmer with substitution, it is related to energy storage properties of ferroelectric materials. Recoverable energy density (W_S ~green area in Fig. 8e), released during discharging process was calculated from P - E loops [50, 51] using:

$$W_S = \int_{P_r}^{P_{Max}} E dP \quad (4)$$

Where, E denotes the applied external electric field, P_{Max} and P_r are the maximum and remnant polarization respectively. Recoverable energy (W_S) increases with the increase in substitution. Hysteresis loss (W_L ~ orange area in Fig. 8e), i.e. unrecoverable energy in the discharging process can be evaluated similarly. Total energy supplied in charging process is $W_{Supplied} = W_S + W_L$. Hence, energy storage efficiency (η) can be defined:

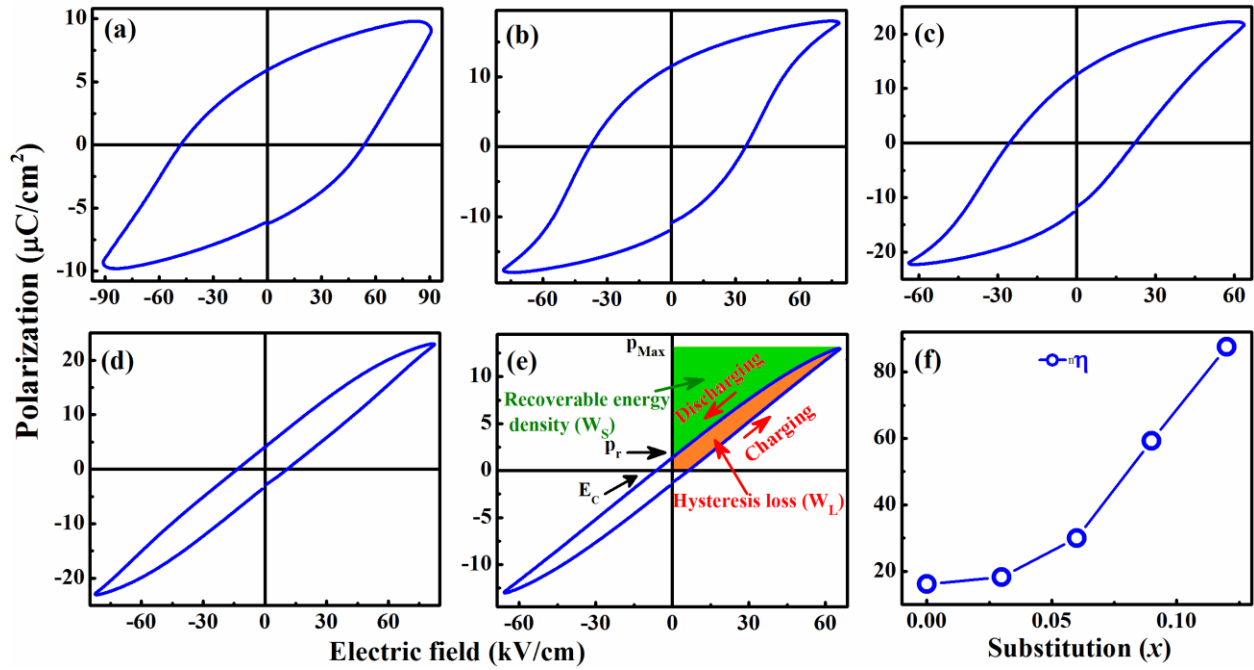


Figure 8. Ferroelectric properties of $(Na_{0.5-x}K_xBi_{0.5-x}La_x)TiO_3$ ($0 \leq x \leq 0.12$) samples, where (a) $x = 0$, (b) $x = 0.03$, (c) $x = 0.06$, (d) $x = 0.09$, (e) $x = 0.12$ is revealed from polarization verses electric field loops. Figure 8e is marked to indicate different parameters used to calculate energy density, and (f) Energy storage efficiency versus composition.

$$\text{Energy storage efficiency } (\eta) = \frac{W_S}{W_{Supplied}} * 100 \quad (5)$$

Energy storage efficiency, η , for NKB LT-x samples [Fig. 8f] increases exponentially with increasing substitution. It is noteworthy to mention that η rises from 17% in NBT to 87 % in $x = 0.12$ sample. Also, lower composition samples can be used in energy conversion devices etc.

Table 4. Ferroelectric properties at room temperature of $(\text{Na}_{0.5-x}\text{K}_x\text{Bi}_{0.5-x}\text{La}_x)\text{TiO}_3$ ($0 \leq x \leq 0.12$) samples.

X	$2E$ (kV/cm)	$2P_r$ ($\mu\text{C}/\text{cm}^2$)	Stored energy (J/cm 3)	E_{Max} (kV/cm)	η (%)
0	95.9	11.84	0.124	90.8	16.15
0.03	76.28	23.09	0.182	78.2	18.26
0.06	51.36	25.04	0.215	63.7	30
0.09	26.8	8.12	0.340	84.2	59.3
0.12	12.68	2.8	0.358	65.7	87.54

Conclusions

In summary, single-phase lead-free ferroelectric $(\text{Na}_{0.5-x}\text{K}_x\text{Bi}_{0.5-x}\text{La}_x)\text{TiO}_3$ ($0 \leq x \leq 0.12$) successfully synthesized by the sol-gel self-combustion method. Structural analysis of synchrotron powder XRD data by Rietveld refinement for all the samples reveals that all compositions belong to rhombohedral crystal structure with $R\bar{3}c$ space group. There is no structural change in samples with composition. Anti-phase octahedral tilting was reduced from 8.47° to 5.89° for $x = 0$ and 0.12 composition respectively. Lattice parameters ' a ' are increased, and ' c ' is decreased, while overall volume increased, the clear indication of successfully substituted because of increase in effective A-site substituted radii. Also, lattice distortion is reduced while disorders are increased with increase in substitution. FESEM micrographs analysis observed that all the samples were well dense with reduced in average grain size with substitution. Room temperature frequency dependent study shows that dielectric constant increases with substitution. A temperature-dependent dielectric study revealed FE to AFE, and AFE to PE phase transitions shifted towards lower temperatures and increase in these diffused anomalies with $\text{K}^+/\text{La}^{3+}$ substitution due to the reduction in distortion with substitution. This provides a stable dielectric constant over a larger temperature range. Thus the materials become more important to be utilized in high-temperature stable capacitor applications due to the enhancement of A-site lattice disorder. Ferroelectricity is observed in all NKB LT-x samples. Energy storage efficiency increased with substitution and was highest $\sim 87\%$ for $x = 0.12$ composition. Result shows that this material has vast scope in high-temperature stable capacitors beyond operating temperature $>200^\circ\text{C}$ with high dielectric constant (for $x = 0.06$ composition

with $\varepsilon_{\text{mid}} \sim 2508 \pm 10\%$ for the temperature range $\sim 180\text{ }^{\circ}\text{C}$ to $340\text{ }^{\circ}\text{C}$) and efficient energy storage applications.

Acknowledgment

Principle investigator expresses thanks to the Indian Institute of Technology Indore, India for funding the research and using Sophisticated Instrument Centre (SIC). Dr. Sajal Biring acknowledges financial support from the Ministry of Science and Technology, Taiwan (MOST 105-2218-E-131-003 and 106-2221-E-131-027). Dr. Sunil Kumar sincerely thanks SERB for Early Career Research award (ECR/2015/0561).

References

- [1] X. Hao, A review on the dielectric materials for high energy-storage application, *J Adv Dielectr*, 03 (2013) 1330001.
- [2] W. Yun-Hsiang, C.L. Yung, S.S. Ganesh, C. Po-Ju, L. Ya-Chu, H. Chih-Fang, K. Wei-Hung, L. Guo-Qiang, High-temperature studies of multiple fluorinated traps within an Al_2O_3 gate dielectric for E-Mode AlGaN/GaN power MIS-HEMTs, *Semicond. Sci. Technol.*, 31 (2016) 025004.
- [3] P.G. Neudeck, R.S. Okojie, C. Liang-Yu, High-temperature electronics - a role for wide bandgap semiconductors?, *Proceedings of the IEEE*, 90 (2002) 1065-1076.
- [4] D. Ma, X. Chen, G. Huang, J. Chen, H. Zhou, L. Fang, Temperature stability, structural evolution and dielectric properties of $\text{BaTiO}_3\text{-Bi}(\text{Mg}_{2/3}\text{Ta}_{1/3})\text{O}_3$ perovskite ceramics, *Ceram. Int.*, 41 (2015) 7157-7161.
- [5] I.V. Smolenskii GA, Agranovskaya AI, Krainik NN, New ferroelectrics of complex composition IV, *Phys Solid State*, 2 (1961) 2651-2654.
- [6] E. Aksel, J.S. Forrester, B. Kowalski, M. Deluca, D. Damjanovic, J.L. Jones, Structure and properties of Fe-modified $\text{Na}_{0.5}\text{Bi}_{0.5}\text{TiO}_3$ at ambient and elevated temperature, *Phys. Rev. B*, 85 (2012) 024121.
- [7] T. Badapanda, S. Sahoo, P. Nayak, Dielectric, Ferroelectric and Piezoelectric study of BNT-BT solid solutions around the MPB region, *IOP Conference Series: Mater. Sci. Eng.*, 178 (2017) 012032.
- [8] M. Li, H. Zhang, S.N. Cook, L. Li, J.A. Kilner, I.M. Reaney, D.C. Sinclair, Dramatic Influence of A-Site Nonstoichiometry on the Electrical Conductivity and Conduction Mechanisms in the Perovskite Oxide $\text{Na}_{0.5}\text{Bi}_{0.5}\text{TiO}_3$, *Chem. Mater.*, 27 (2015) 629-634.
- [9] S. Kim, H. Choi, S. Han, J.S. Park, M.H. Lee, T.K. Song, M.-H. Kim, D. Do, W.-J. Kim, A correlation between piezoelectric response and crystallographic structural parameter observed in lead-free $(1-x)(\text{Bi}_{0.5}\text{Na}_{0.5})\text{TiO}_3\text{-}x\text{SrTiO}_3$ piezoelectrics, *J. Eur. Ceram. Soc.*, 37 (2017) 1379-1386.
- [10] W. Jo, R. Dittmer, M. Acosta, J. Zang, C. Groh, E. Sapper, K. Wang, J. Rödel, Giant electric-field-induced strains in lead-free ceramics for actuator applications – status and perspective, *J. Electroceram.*, 29 (2012) 71-93.
- [11] E. Aksel, J.L. Jones, Advances in Lead-Free Piezoelectric Materials for Sensors and Actuators, *Sensors* (Basel, Switzerland), 10 (2010) 1935-1954.
- [12] M.K. Niranjan, T. Karthik, S. Asthana, J. Pan, U.V. Waghmare, Theoretical and experimental investigation of Raman modes, ferroelectric and dielectric properties of relaxor $\text{Na}_{0.5}\text{Bi}_{0.5}\text{TiO}_3$, *J. Appl. Phys.*, 113 (2013) 194106.
- [13] B.N. Rao, R. Datta, S.S. Chandrashekaran, D.K. Mishra, V. Sathe, A. Senyshyn, R. Ranjan, Local structural disorder and its influence on the average global structure and polar properties in $\text{Na}_{0.5}\text{Bi}_{0.5}\text{TiO}_3$, *Phys. Rev. B*, 88 (2013) 224103.

[14] U.V. Waghmare, N.A. Spaldin, H.C. Kandpal, R. Seshadri, First-principles indicators of metallicity and cation off-centricity in the IV-VI rocksalt chalcogenides of divalent Ge, Sn, and Pb, *Phys. Rev. B*, 67 (2003) 125111.

[15] M. Yashima, K. Omoto, J. Chen, H. Kato, X. Xing, Evidence for (Bi,Pb)-O Covalency in the High T_c Ferroelectric PbTiO_3 - BiFeO_3 with Large Tetragonality, *Chem. Mater.*, 23 (2011) 3135-3137.

[16] A.K. Yadav, P. Rajput, O. Alshammari, M. Khan, Anita, G. Kumar, S. Kumar, P.M. Shirage, S. Biring, S. Sen, Structural distortion, ferroelectricity and ferromagnetism in $\text{Pb}(\text{Ti}_{1-x}\text{Fe}_x)\text{O}_3$, *J. Alloys Compd.*, 701 (2017) 619-625.

[17] G. Laurita, K. Page, S. Suzuki, R. Seshadri, Average and local structure of the Pb-free ferroelectric perovskites $(\text{Sr},\text{Sn})\text{TiO}_3$ and $(\text{Ba},\text{Ca},\text{Sn})\text{TiO}_3$, *Phys. Rev. B*, 92 (2015) 214109.

[18] X. Chou, J. Zhai, H. Jiang, X. Yao, Dielectric properties and relaxor behavior of rare-earth (La, Sm, Eu, Dy, Y) substituted barium zirconium titanate ceramics, *J. Appl. Phys.*, 102 (2007) 084106.

[19] F. Yang, H. Zhang, L. Li, I.M. Reaney, D.C. Sinclair, High Ionic Conductivity with Low Degradation in A-Site Strontium-Doped Nonstoichiometric Sodium Bismuth Titanate Perovskite, *Chem. Mater.*, 28 (2016) 5269-5273.

[20] C.E. Mohn, S. Stølen, Influence of the stereochemically active bismuth lone pair structure on ferroelectricity and photocatalytic activity of Aurivillius phase Bi_2WO_6 , *Phys. Rev. B*, 83 (2011) 014103.

[21] Y. Yuan, X.H. Zhou, C.J. Zhao, B. Li, S.R. Zhang, High-Temperature Capacitor Based on Ca-Doped $\text{Bi}_{0.5}\text{Na}_{0.5}\text{TiO}_3$ - BaTiO_3 Ceramics, *J. Electron. Mater.*, 39 (2010) 2471-2475.

[22] I. Levin, I.M. Reaney, Nano- and Mesoscale Structure of $\text{Na}_{1-x}\text{Bi}_{1-x}\text{TiO}_3$: A TEM perspective, *Adv. Funct. Mater.*, 22 (2012) 3445-3452.

[23] A.A. Bokov, L.A. Shpak, I.P. Rayevsky, Diffuse phase transition in $\text{Pb}(\text{Fe}0.5\text{Nb}0.5)\text{O}_3$ -based solid solutions, *J. Phys. Chem. Solids*, 54 (1993) 495-498.

[24] S. Swain, P. Kumar, D.K. Agrawal, Sonia, Dielectric and ferroelectric study of KNN modified NBT ceramics synthesized by microwave processing technique, *Ceram. Int.*, 39 (2013) 3205-3210.

[25] K. Bridger, A.V. Cooke, W.A. Schulze, High-Temperature Dielectric Materials and Capacitors Made Therefrom, Google Patents, 2008.

[26] A. Zeb, S.u. Jan, F. Bamiduro, D.A. Hall, S.J. Milne, Temperature-stable dielectric ceramics based on $\text{Na}_{0.5}\text{Bi}_{0.5}\text{TiO}_3$, *J. Eur. Ceram. Soc.*, 38 (2018) 1548-1555.

[27] V. Koch, D. Andrae, Static electric dipole polarizabilities for isoelectronic sequences. II. Open-shell S states, *Eur. Phys. J. D*, 67 (2013) 139.

[28] K. Sunil, K.B.R. Varma, Influence of lanthanum doping on the dielectric, ferroelectric and relaxor behaviour of barium bismuth titanate ceramics, *J. Phys. D: Appl. Phys.*, 42 (2009) 075405.

[29] V. Srihari, V. Sridharan, H.K. Sahu, G. Raghavan, V.S. Sastry, C.S. Sundar, Combustion synthesis of Ga_2O_3 nanoparticles, *J Mater. Sci. Eng.*, 44 (2009) 671-675.

[30] A.P. Hammersley, S.O. Svensson, M. Hanfland, A.N. Fitch, D. Hausermann, Two-dimensional detector software: From real detector to idealised image or two-theta scan, *High Pressure Research*, 14 (1996) 235-248.

[31] H.D. Megaw, C.N.W. Darlington, Geometrical and structural relations in the rhombohedral perovskites, *Acta Cryst. A*, 31 (1975) 161-173.

[32] J. Rodriguez-Carvajal, FULLPROF: A Program for Rietveld Refinement and Pattern Matching Analysis Toulouse, France, 1990, pp. 127.

[33] A. Yoshiasa, T. Nakatani, A. Nakatsuka, M. Okube, K. Sugiyama, T. Mashimo, High-temperature single-crystal X-ray diffraction study of tetragonal and cubic perovskite-type PbTiO_3 phases, *Acta Crystallogr., Sect. B*, 72 (2016) 381-388.

[34] S. Rachna, S. Gurvinderjit, S. Vasant, V.S. Tiwari, P.K. Gupta, Dielectric, structural and Raman studies on $(\text{Na}_{0.5}\text{Bi}_{0.5}\text{TiO}_3)_{(1-x)}(\text{BiCrO}_3)_x$ ceramic, *J. Phys.: Condens. Matter*, 23 (2011) 055901.

[35] P.A.T. G.O. Jones, Investigation of the structure and phase transitions in the novel A-site substituted distorted perovskite compound $\text{Na}_{0.5}\text{Bi}_{0.5}\text{TiO}_3$, *Acta Crystallogr. B*, 58 (2002) 168-178.

[36] K. Momma, F. Izumi, VESTA: a three-dimensional visualization system for electronic and structural analysis, *J. Appl. Crystallogr.*, 41 (2008) 653-658.

[37] N.A. Benedek, C.J. Fennie, Why Are There So Few Perovskite Ferroelectrics?, *J. Phys. Chem. C*, 117 (2013) 13339-13349.

[38] A.K. Yadav, Anita, S. Kumar, A. Panchwanee, V.R. Reddy, P.M. Shirage, S. Biring, S. Sen, Structural and ferroelectric properties of perovskite $\text{Pb}_{(1-x)}(\text{K}_{0.5}\text{Sm}_{0.5})_x\text{TiO}_3$ ceramics, *RSC Adv.*, 7 (2017) 39434-39442.

[39] C.H. Hsueh, A.G. Evans, R.L. Coble, Microstructure development during final/intermediate stage sintering—I. Pore/grain boundary separation, *Acta Metall.*, 30 (1982) 1269-1279.

[40] S. Sayyed, S.A. Acharya, P. Kautkar, V. Sathe, Structural and dielectric anomalies near the MPB region of $\text{Na}_{0.5}\text{Bi}_{0.5}\text{TiO}_3$ - SrTiO_3 solid solution, *RSC Adv.*, 5 (2015) 50644-50654.

[41] V. Pal, R.K. Dwivedi, O.P. Thakur, Synthesis and ferroelectric behavior of Gd doped BNT ceramics, *Curr. Appl. Phys.*, 14 (2014) 99-107.

[42] W. Ji, X. He, W. Cheng, P. Qiu, X. Zeng, B. Xia, D. Wang, Effect of La content on dielectric, ferroelectric and electro-optic properties of $\text{Pb}(\text{Mg}_{1/3}\text{Nb}_{2/3})\text{O}_3$ - PbTiO_3 transparent ceramics, *Ceram. Int.*, 41 (2015) 1950-1956.

[43] L. Liu, D. Shi, Y. Huang, S. Wu, X. Chen, L. Fang, C. Hu, Quantitative Description of the Diffuse Phase Transition of BNT-NKN Ceramics, *Ferroelectr.*, 432 (2012) 65-72.

[44] A.K. Yadav, Anita, S. Kumar, V.R. Reddy, P.M. Shirage, S. Biring, S. Sen, Structural and dielectric properties of $\text{Pb}_{(1-x)}(\text{Na}_{0.5}\text{Sm}_{0.5})_x\text{TiO}_3$ ceramics, *J. Mater. Sci. Mater. Electron.*, 28 (2017) 10730-10738.

[45] A. Zeb, S.J. Milne, High temperature dielectric ceramics: a review of temperature-stable high-permittivity perovskites, *J. Mater. Sci. Mater. Electron.*, 26 (2015) 9243-9255.

[46] P. Zheng, J.L. Zhang, Y.Q. Tan, C.L. Wang, Grain-size effects on dielectric and piezoelectric properties of poled BaTiO_3 ceramics, *Acta Mater.*, 60 (2012) 5022-5030.

[47] Y. Tan, J. Zhang, Y. Wu, C. Wang, V. Koval, B. Shi, H. Ye, R. McKinnon, G. Viola, H. Yan, Unfolding grain size effects in barium titanate ferroelectric ceramics, *Sci. Rep.*, 5 (2015) 9953.

[48] J.P. Praveen, K. Kumar, A.R. James, T. Karthik, S. Asthana, D. Das, Large piezoelectric strain observed in sol-gel derived BZT-BCT ceramics, *Curr. Appl. Phys.*, 14 (2014) 396-402.

[49] C.A. Randall, N. Kim, J.-P. Kucera, W. Cao, T.R. Shrout, Intrinsic and Extrinsic Size Effects in Fine-Grained Morphotropic-Phase-Boundary Lead Zirconate Titanate Ceramics, *J. Am. Ceram. Soc.*, 81 (1998) 677-688.

[50] X. Lu, J. Xu, L. Yang, C. Zhou, Y. Zhao, C. Yuan, Q. Li, G. Chen, H. Wang, Energy storage properties of $(\text{Bi}_{0.5}\text{Na}_{0.5})_{0.93}\text{Ba}_{0.07}\text{TiO}_3$ lead-free ceramics modified by La and Zr co-doping, *J. Materiomics.*, 2 (2016) 87-93.

[51] Y. Wu, Y. Hu, X. Wang, C. Zhong, L. Li, Temperature- and frequency-dependent dielectric response and energy-storage performance in high (100)-oriented Sc doped $(\text{Na}_{0.85}\text{K}_{0.15})_{0.5}\text{Bi}_{0.5}\text{TiO}_3$ films, *RSC Adv.*, 7 (2017) 51485-51494.